Supplementary Information

Utilizing the synergistic effect between Schottky barrier and field redistribution to achieve high-density, low-consumption cellulose-based flexible dielectric films —for next-generation green energy storage capacitors

Zixiong Sun[a,b,c,d,e], Hansong Wei[b], Shibo Zhao[a], Qing Guo[a], Yuhan Bai[a], Siting Wang[a], Peiyao Sun[f], Kang Du[g], Yating Ning[h], Ye Tian[h], Xiaohua Zhang[h], Hongmei Jing[i], Yongping Pu[h], Sufeng Zhang[b*]*

a School of Electronic Information and Artificial Intelligence, Shaanxi University of Science and Technology, Xi'an 710021, PR China

b Shaanxi Provincial Key Laboratory of Papermaking Technology and Specialty Paper Development, National Demonstration Center for Experimental Light Chemistry Engineering Education, Key Laboratory of Paper Based Functional Materials of China National Light Industry, Shaanxi University of Science and Technology, Xi'an, 710021, PR China

c Key Laboratory of Auxiliary Chemistry and Technology for Chemical Industry, Ministry of Education, Shaanxi University of Science and Technology, Xi'an 710021, PR China

d Shaanxi Collaborative Innovation Center of Industrial Auxiliary Chemistry and Technology, Shaanxi University of Science and Technology, Xi'an 710021, China

e MESA$^+$ Institute for Nanotechnology, University of Twente PO Box 217, 7522 NH Enschede, The Netherlands

f Department of Biology, Shenzhen MSU-BIT University, Shen Zhen, China

g School of Mathematical and Physical Sciences, Wuhan Textile University, Wuhan, 430200, China

h School of Materials Science and Engineering, Shaanxi University of Science and Technology, Xi'an 710021, PR China

i School of Physics and Information Technology, Shaanxi Normal University, Xi'an, 710119, PR China

**Corresponding author: Zixiong Sun, Sufeng Zhang*

E-mail address: SunZX@sust.edu.cn, zhangsufeng@sust.edu.cn

1. Experimental Section

1.1. Materials

The cellulose comes from the cotton linter purchased from Hubei Jinhuan New Material Technology Co., Ltd. The Dimethylacetamide (DMAc) solutions (99.0%), lithium chloride (LiCl, 99.0%), polyvinylidene fluoride (PVDF), titanium tetrachloride ($TiCl_4$), zirconium oxychloride ($ZrOCl_2 \cdot 8H_2O$), strontium nitrate ($Sr(NO_3)_2$), sodium hydroxide (NaOH), and barium chloride dihydrate ($BaCl_2 \cdot 2H_2O$) were all purchased from Sinopharm Chemical Reagent Co., Ltd.

1.2. Preparation of BZT and BST ceramic fillers by hydrothermal method

$BaZr_{0.2}Ti_{0.8}O_3$ (BZT) and $Ba_{0.4}Sr_{0.6}TiO_3$ (BST) inorganic nano-ceramic fillers were prepared through the hydrothermal method, with the raw materials of $BaCl_2 \cdot 2H_2O$, $ZrOCl_2 \cdot 8H_2O$, $Sr(NO_3)_2$ and $TiCl_4$. First, $BaCl_2 \cdot 2H_2O$(*s*, 4.88 g) and $ZrOCl_2 \cdot 8H_2O$(*s*, 1.29 g) were added into deionized water of 20 ml and 10 ml separately, and the solutions were stirred at room temperature until the powders were completely dissolved. Then, mixed them and added $TiCl_4$(*l*, 1.76 ml) drop by drop until completely dissolved. To prevent HCl(*g*) volatilization, this process can be done in frozen-water circumstances. The precursor of BZT and BST were then obtained by adding proper quality of NaOH(*s*) with severe reactions. After a standing of ~10 min, the obtained BZT and BST precursor were transferred to the hydrothermal reactors, and a hydrothermal reaction was carried out at 200 ^oC for 12 h. When the reactions finished, the powders were transferred to 2L beakers full of deionized water and started a washing process with the repetition of over five times to remove the Cl^{-1}. After this, BZT and BST powder can be obtained after drying at 80 ^oC for 24 h.

1.3. Preparation of precursors RC/PVDF-BZT and RC/PVDF-BST

The manufacturing process of RC/PVDF-BZT and RC/PVDF-BST precursors follows the techniques of our previous work[1]. In brief, the transparent cellulose solution dissolved by DMAc and the PVDF dissolved by DMAc were mixed according to the mass ratio 4:1 to get the RC/PVDF mixture. Then, the as-prepared BZT and BST particles obtained from the hydrothermal method mentioned above were added with a volume fraction of 2%. The ternary solution doped with two different BZT and BST fillers should be stirred for at least 12 h until evenly mixed. Finally, the precursors RC/PVDF-BZT and RC/PVDF-BST doped with different fillers were obtained by ultrasonic oscillation-assisted magnetic stirring for 30 minutes, repeated six times.

1.4. Preparation of monolayer and multilayer films

Using the precursors obtained above, conventional tape-casting technology was employed for BZT and BST single layers. The final thickness of the prepared films was controlled to be ~15 μm. For the multilayer-structured films, the thickness of each sublayer was controlled to be ~5 μm, and by regulating the tape-casting sequence, the films with the structure of ZZS, ZSZ, SSZ, and SZS were obtained. To avoid the effect of the hydrogen bond network self-assembly on the interface between adjacent sublayers, the casting process of each *next layer* must be started before the *previous layer* is completely dry. This is a trick that deserves many attempts to find the correct time, and according to the cross-sectional SEM images in this manuscript, the multilayer-structured films in our work are all very dense without any noticeable pores inside.

1.5. Characterization

The crystalline structure of all the multilayers was measured by X-ray diffraction (XRD Rigaku D/max-2200PC). Scanning electron microscopy (SEM Thermo Fisher Scientific) and transmission electron microscopy (FE-TEM, JEOL, JEM-F200) were used to measure the microstructure of the cross-sectional and lattice fringe of the film samples. The Fourier transform infrared spectroscopy (FTIR, Spotlight 400 & Frontier) was employed to identify the functional groups of multilayers. Both the frequency dependence of the dielectric constant (ε) with dielectric loss ($tan\delta$) and temperature dependence of the ε with $tan\delta$ were obtained from the impedance analyzer (E4980A, Agilent). The XPS data was performed using an Omicron Argus spectrometer (Taunusstein, Germany) equipped with a monochromated Al $K\alpha$ radiation source (hv=1486,6 eV) working at an electron beam power of 300 W. The *J-E curves* and hysteresis loops (*P-E loops*) were measured using a ferroelectric tester (Radiant Premier II), and the dynamic discharging performances were obtained from a charging-discharging measurement system (Tongguo technology, CFD-003, China). The surface contact angles of composite samples were measured by an optical contact angle machine (OCA20, Dataphysics), and the servo control system universal testing machine (AI-7000-NGD, Gotech Testing Machines) was employed for measuring the mechanical properties.

2. Details of the *Rietveld* XRD refinement

The R_{wp} and *Rp* are the weighted profile parameters and unweighted profile parameters for fitting each powder, respectively. Based on their values, our refinement result is quite convincing[2].

Tab. S1 lattice parameters of the BZT and BST particles obtained from the XRD refinement.

powders / Lattice parameter	BZT	BST
a (Å)	4.046	3.941
b (Å)	4.046	3.941
c (Å)	4.103	3.941
c/*a* ratio	1.014	1.000
V (Å^3)	67.167	61.210
R_p	7.15	7.75
R_{wp}	9.72	9.83

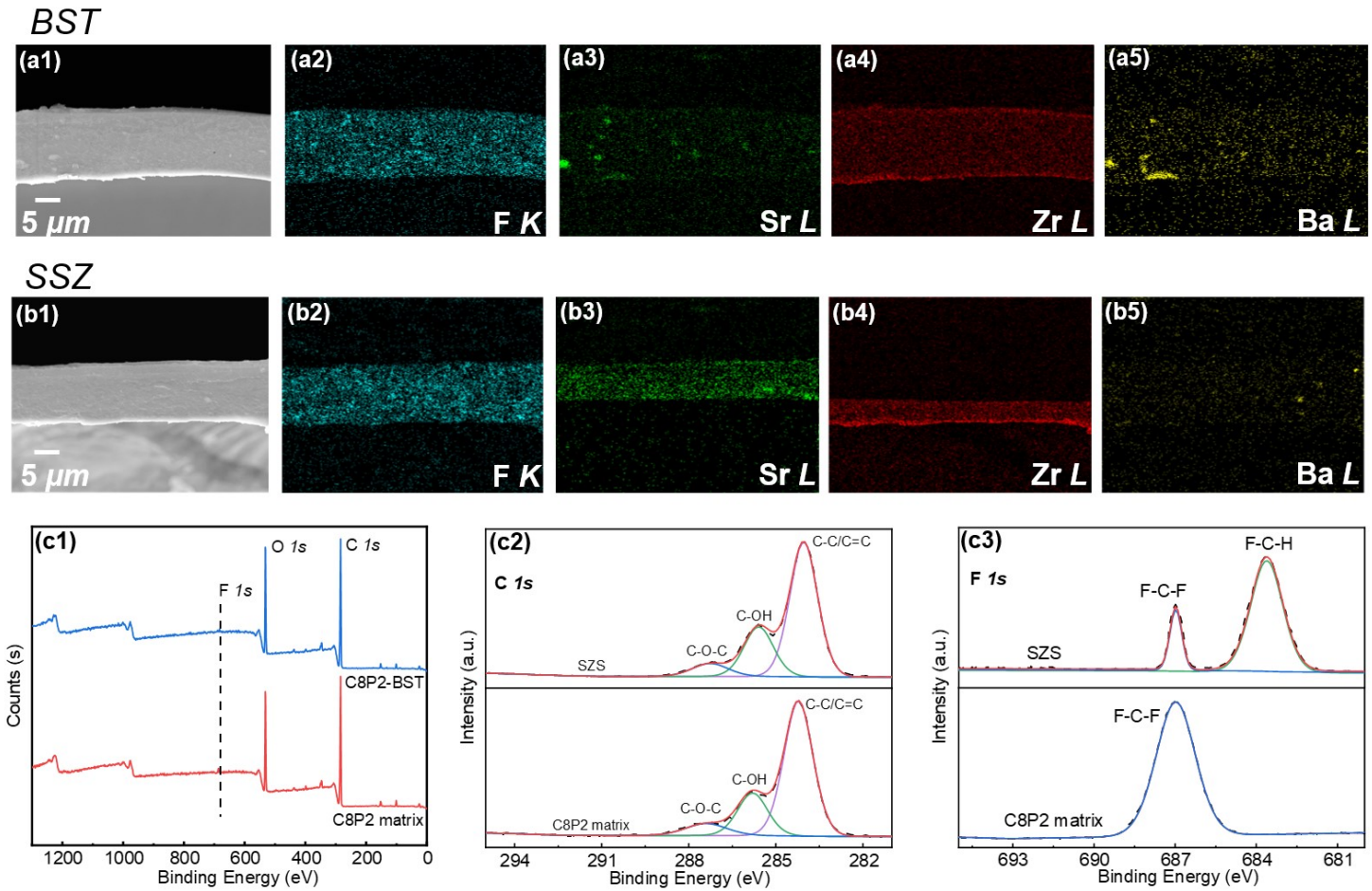

Fig. S1 (a1) cross-sectional SEM image; (a2)-(a5) the EDS mapping for F-*K*, Sr-*L*, Zr-*L*, and Ba-*L* of the BST; (b12) cross-sectional SEM image; (b2)-(b5) the EDS mapping for F-*K*, Sr-*L*, Zr-*L*, and Ba-*L* of the SSZ; (c1) XPS spectra from 0 eV to 1300 eV; (c2) slow scanning XPS spectra at *C1s*; (c3) slow scanning XPS spectra at *F1s* of both the C8P2 matrix and the SZS.

3. Wei-bull Distribution

Before calculating the energy storage density(ESD), the electric breakdown strength(E_b) of each film should be confirmed by employing the *Weibull* distribution, which can be expressed as follows:

$$X_i = \ln E_i \quad \text{Eq. S1}$$

$$Y_i = \ln(- \ln (1 - P_i)) \quad \text{Eq. S2}$$

$$P_i = \frac{i}{1 + n} \quad \text{Eq. S3}$$

where X_i and Y_i are the two parameters of the Weibull distribution, Y_i varies linearly with X_i with a slope of β, $E_{i,}$ and P_i are the sample's breakdown field and the electric field's failure probability distribution, respectively. While n, i, and β are the total number of specimens, the serial number of dielectric strength, and the slope of the linear relationship between ln(E_i) and ln(-ln(1-P_i)), respectively.

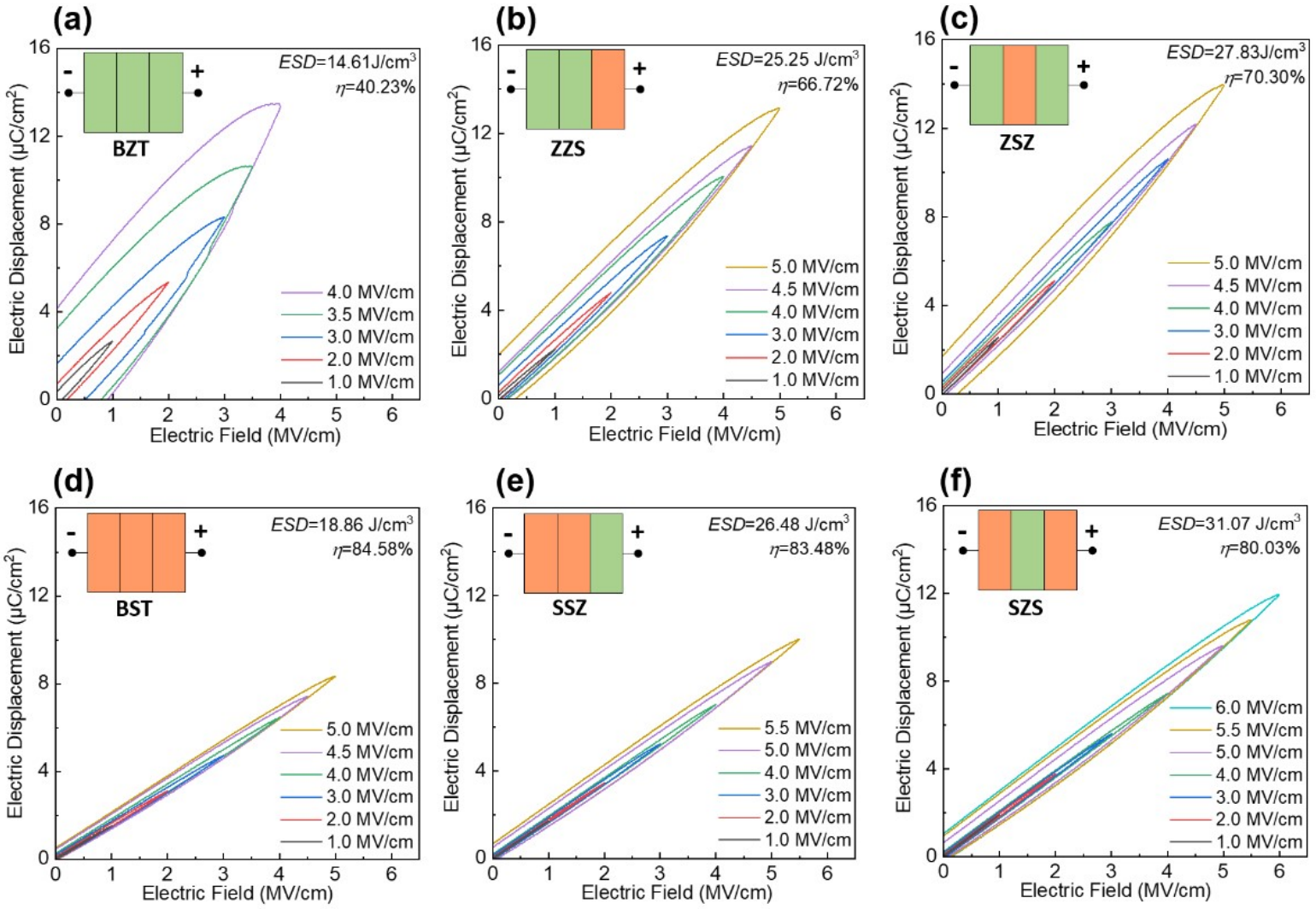

Fig. S2 (a)-(f) *P-E* loops of all the films measured under different electric fields.

4. Calculation of *ESD* and η

The energy storage density(*ESD*) and η of a dielectric capacitor under a specific applied electrical field (*E*) can be represented by the following formula:

$$W_{\text{rec}} = \int_{P_{\text{m}}}^{P_{\text{r}}} E\text{d}P \qquad \text{Eq. S4}$$

$$W_{\text{char}} = \int_{0}^{P_{\text{m}}} E\text{d}P \qquad \text{Eq. S5}$$

$$\eta = W_{rec}/W_{sto} * 100\% \qquad \text{Eq. S6}$$

in which the W_{rec} and $W_{char,}$ are the *ESD* and energy-charged density(*ECD*) during one charge-discharge process, respectively. In a complete charge-discharge circle, the polarization goes up along the OAB with increasing voltage and goes down along the BCD when the voltage drops. The *ESD* represents the dashed area in Fig. S3(a), and the *ECD* represents the sum of the dashed area and solid area. The solid area covered by the *P*-*E* loops means the energy loss during one charge-discharge circle. The energy efficiency (η) is expressed by the division between *ESD* and *ECD*, as inserted in the figure. *P* is the generated polarization under *E*, and the P_m and P_r are the maximum polarization upon charging and the remanent polarization when the electrical field returns to zero, respectively.

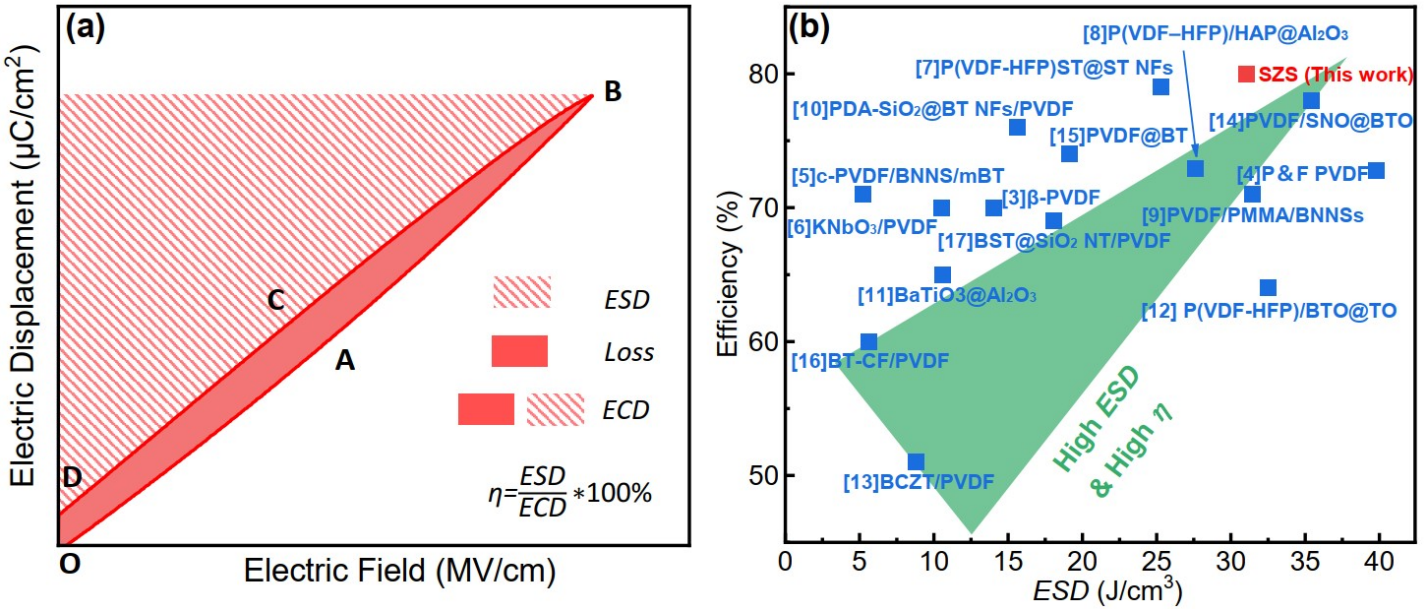

Fig. S3(a) sketch to show the ESD, ECD, loss, and η in a P-E loop in this work; (b) the comparison of ESD and η between our films and typical PVDF-based dielectric capacitors that were reported in the latest five years[3-17].

5. The physical meaning of the abbreviations in the band diagram analyzing

E_{VAC}: the vacuum level

E_{FA}: the Fermi energy level of Au

$E_{FZ}/E_{F\text{-}ZZS}/E_{F\text{-}ZSZ}/E_{FS}/E_{F\text{-}SSZ}/E_{F\text{-}SZS}$:

the equivalent Fermi energy level of the BZT layer/ZZS/ZSZ/BST layer/SSZ/SZS

$E_{CZ}/E_{C\text{-}ZZS}/E_{C\text{-}ZSZ}/E_{CS}/E_{C\text{-}SSZ}/E_{C\text{-}SZS}$:

the equivalent conduction band of the BZT layer/ZZS/ZSZ/BST layer/SSZ/SZS

$E_{VZ}/E_{V\text{-}ZZS}/E_{C\text{-}ZSZ}/E_{CS}/E_{C\text{-}SSZ}/E_{C\text{-}SZS}$:

the equivalent conduction band of the BZT layer/ZZS/ZSZ/BST layer/SSZ/SZS

ϕ_A: the work function of Au

$\phi_Z/\phi_{ZZS}/\phi_{ZSZ}/\phi_S/\phi_{SSZ}/\phi_{SZS}$:

the equivalent work function of the BZT layer/ZZS/ZSZ/BST layer/SSZ/SZS

$\chi_Z/\chi_{ZZS}/\chi_{ZSZ}/\chi_S/\chi_{SSZ}/\chi_{SZS}$:

the equivalent electron affinity of the BZT layer/ZZS/ZSZ/BST layer/SSZ/SZS

ϕ_s: the Schottky barrier height

ϕ_b: the build-in potential

V: the applied voltage

V_Z: the voltage applied on BZT single layer

V_Z'/V_Z'': the voltage applied on the BZT sublayer that connected to Au in ZZS/ZSZ

V_S: the voltage applied on BST single layer

V_S'/V_S'': the voltage applied on the BST sublayer that connected to Au in SSZ/SZS

$D_{A\text{-}Z}/D_{A\text{-}Z}'/D_{A\text{-}Z}''/D_{A\text{-}Z}'''$: the depletion layer in Au/BZT interface on BZT single layer after contact without applied voltage/BZT single layer with applied voltage/ZZS with applied voltage/ZSZ with applied voltage

$D_{A\text{-}S}/D_{A\text{-}S}'/D_{A\text{-}S}''/D_{A\text{-}S}'''$: the depletion layer in Au/BST interface on BST single layer after contact without applied voltage/BST single layer with applied voltage/SSZ with applied voltage/SZS with applied voltage

6. Discussions of the Band Bending

Fig. S4(a1) and (b1) show the band diagram of the Au/BZT and Au/BST interface in the BZT single layer and BST single layer before contact, respectively. Here the '*BZT single layer*' and '*BST single layer*' refer to single-layer-structured cellulose/PVDF-$BaZr_{0.2}Ti_{0.8}O_3$ film, and cellulose/PVDF-$Ba_{0.6}Sr_{0.4}TiO_3$ film, respectively. As the Au work function is higher than the electron affinity of both BZT and BST single layer, once connected, in the BZT single layer, for example, the Fermi level of both Au and BZT should be aligned, which leads to the band bending in the interface. Considering the conducting behavior of these composite films should be dominated by the fillers, which are always regarded as *n*-type semiconductors with the major carriers of electrons[18], the electrons would drift from the BZT side to the Au side. Finally, a build-in potential(Φ_b) and a depletion layer($D_{A\text{-}Z}$) with the direction pointing to Au formed in the interface, as displayed in Fig. S4 (a2). When applying a forward voltage pointing from film to electrode, as seen in Fig. S4 (a3), the BZT Fermi level moves down, increasing the Φ_b to (Φ_b+V_Z) and ($D_{A\text{-}Z}$) to ($D_{A\text{-}Z'}$). A similar condition happens in the BST single layer, as demonstrated in Fig. S4(b2) and (b3). The difference between these two conditions is that compared to the BZT single layer, the BST single layer has larger electron affinity and narrower bandgap[19], so the depletion layer after connection in the BST single layer($D_{A\text{-}S}$) is broader than $D_{A\text{-}Z}$, and the E_{FS} moves down to a lower level than the E_{FZ} when under a forward voltage

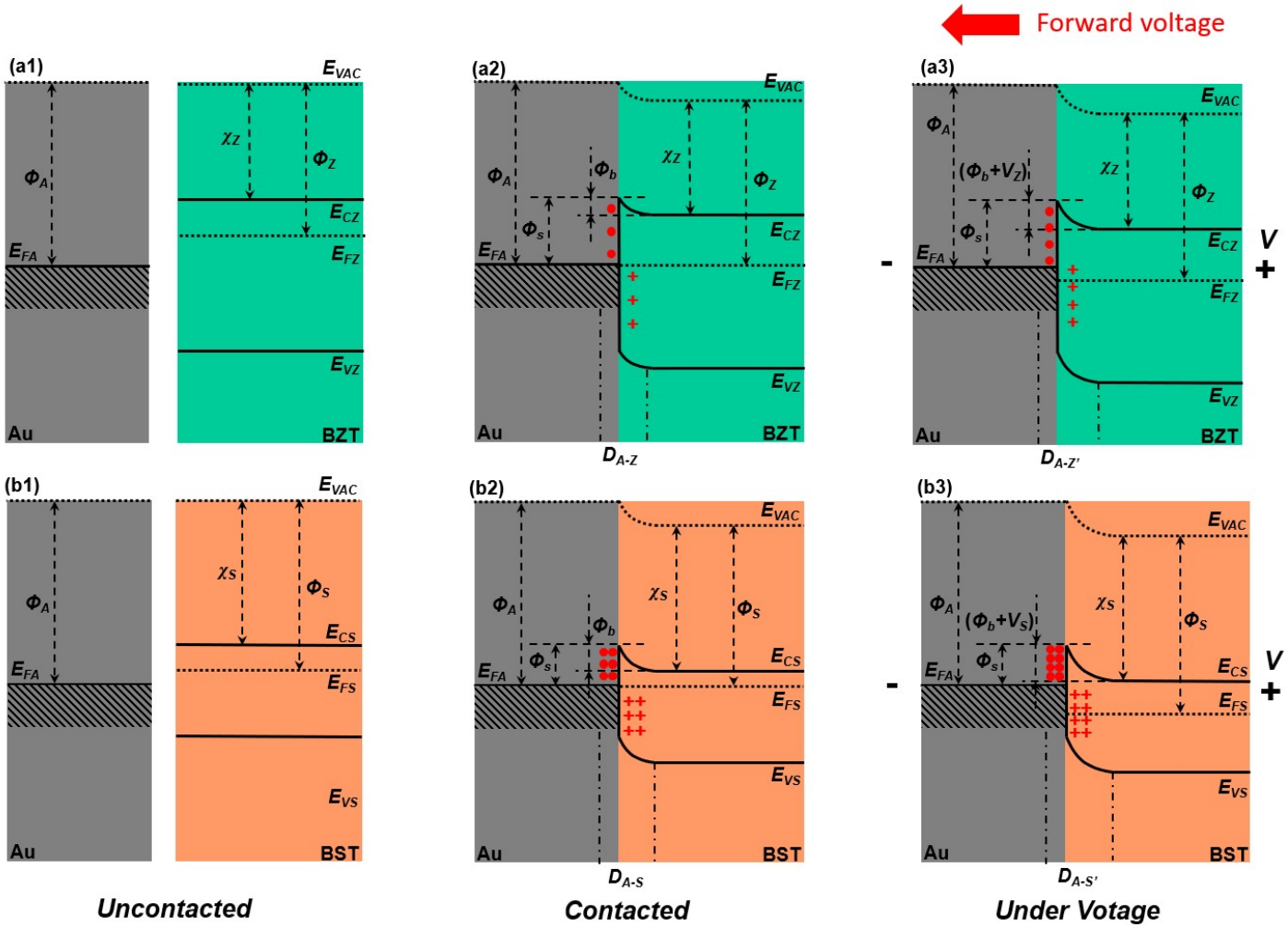

Fig. S4 band diagram of the Au/BZT interface in the BZT single layer (a1) before contact; (a2) after contact; (a3) under forward voltage; band diagram of the Au/BST interface in the BST single layer (b1) before contact; (b2) after contact; (b3) under forward voltage;

7. Finite Element Simulation

The *COMSOLMultiphysics6.0* was employed for simulating the potential and electric field distribution and the current spread. Once the breakdown happens, the film will undergo an irreversible transformation, widely believed to be the joint effect of electric and thermal fields. Based on this, the *AC/DC module* and *heat transfer module* in *COMSOLMultiphysics6.0* are both called, and the physical model can be expressed as follows:

The electrical breakdown process was described according to the spread of current density with the boundary conditions meeting:

$$\boldsymbol{n}\cdot\boldsymbol{i}=0 \qquad \text{Eq. S7}$$

where $\boldsymbol{n}$ and $\boldsymbol{i}$ are the normal vector and current density vector, respectively. This boundary condition means that no electric current flows into the boundary. The constitutive relations are expressed as:

$$\boldsymbol{J}=\sigma\boldsymbol{E} \qquad \text{Eq. S8}$$

which is the standard *Ohm's law* and

$$\boldsymbol{D}=\varepsilon_0\varepsilon_r\boldsymbol{E} \qquad \text{Eq. S9}$$

where $\boldsymbol{J}$ and $\boldsymbol{E}$ are the current density and external electrical field, respectively, and σ and ε_r are each material's electrical conductivity and dielectric constant (permittivity), which needs input in the model. ε_0 is vacuum permittivity with a value of $8.854187817*10^{-12}$ F/m. Considering the stationary equation of continuity of the model after a long time, Eq. S8 should be changed to a more general form:

$$\boldsymbol{J}=\sigma\boldsymbol{E}+\frac{\partial\boldsymbol{D}}{\partial t}+\boldsymbol{J}_e \qquad \text{Eq. S10}$$

At the same time, current conservation should be met from then on with the equations:

$$\nabla \cdot \boldsymbol{J} = Q_{j.v} \quad \text{Eq. S11}$$

$$\boldsymbol{E} = -\nabla V \quad \text{Eq. S12}$$

where $Q_{j.v}$ and $\boldsymbol{D}$ represent the change rate of electric charge per unit volume and the electric displacement vector. $\boldsymbol{J_e}$ is the current density and density of the external electric current, and V denotes the electrical potential. Here, we use the *If sentence*, which is written as *if(ht. alpha>0.1,6e6,0.04)* and was input in the software to determine if a breakdown occurred or not. It means if the breakdown happens, the σ takes the 6e6; otherwise, it takes 0.04. The *ht. alpha* is the physical name of $\frac{\partial \alpha}{\partial t}$, which represents an anisotropic thermal diffusivity(α).

The heat transfer in solid interface solves for the following equation derived from:

$$d_z(\rho C_p)_{eff}\frac{\partial T}{\partial t} + d_z(\rho C_p)_{\text{eff}}\boldsymbol{u}\cdot\nabla T + \nabla\cdot\boldsymbol{q} = d_z Q + q_0 + d_z Q_{ted} \quad \text{Eq. S13}$$

in which the $\boldsymbol{u}$ is the fluid velocity vector, and the $\boldsymbol{q}$ is the conductive heat flux that is written as:

$$\boldsymbol{q} = -d_z k_{eff}\nabla T \quad \text{Eq. S14}$$

and the d_z, $k_{eff,}$ and ∇T are the thickness of the domain in the out-of-plane direction, effective thermal conductivity, and temperature perturbation, respectively. The $(\rho Cp)_{eff}$ is the effective volumetric heat capacity at constant pressure that is composed of two parts:

$$(\rho C_p)_{eff} = \theta_{it} k_{it} + (1 - \theta_{it})k \quad \text{Eq. S15}$$

where the θ_{it} and k are the fraction of transformation and thermal conductivity, respectively, and the θ_{it} can be expressed as:

$$\theta it = \min(\alpha_b, 1) \quad \text{Eq. S16}$$

where the α_b is the fraction of film that was broken down to correspond to the whole film. The

Q in Eq. S13 is the heat source and is defined as:

$$Q = -\rho L_{it,h} \frac{\partial \theta_{it}}{\partial t} (T > T_{it.h}) \quad \text{Eq. S17}$$

where the T_{it}, t_{it}, and L_{it} are the transformation temperature, transformation time, and the enthalpy change when the electric breakdown happens.

The following formula should be satisfied when the *heat transfer module* is coupled with the *AC/DC module*.

$$\frac{\partial \alpha}{\partial t} = \frac{1}{t_{it,h}} (T > T_{it,h}) \quad \text{Eq. S18}$$

Once the electric breakdown happens, the $\frac{\partial \alpha}{\partial t}$ changes, so the σ mentioned above also changes. In our work, the T_{it} and t_{it} are set to be 150 ^{o}C and 0.01ns, respectively, according to the literature[20-22].

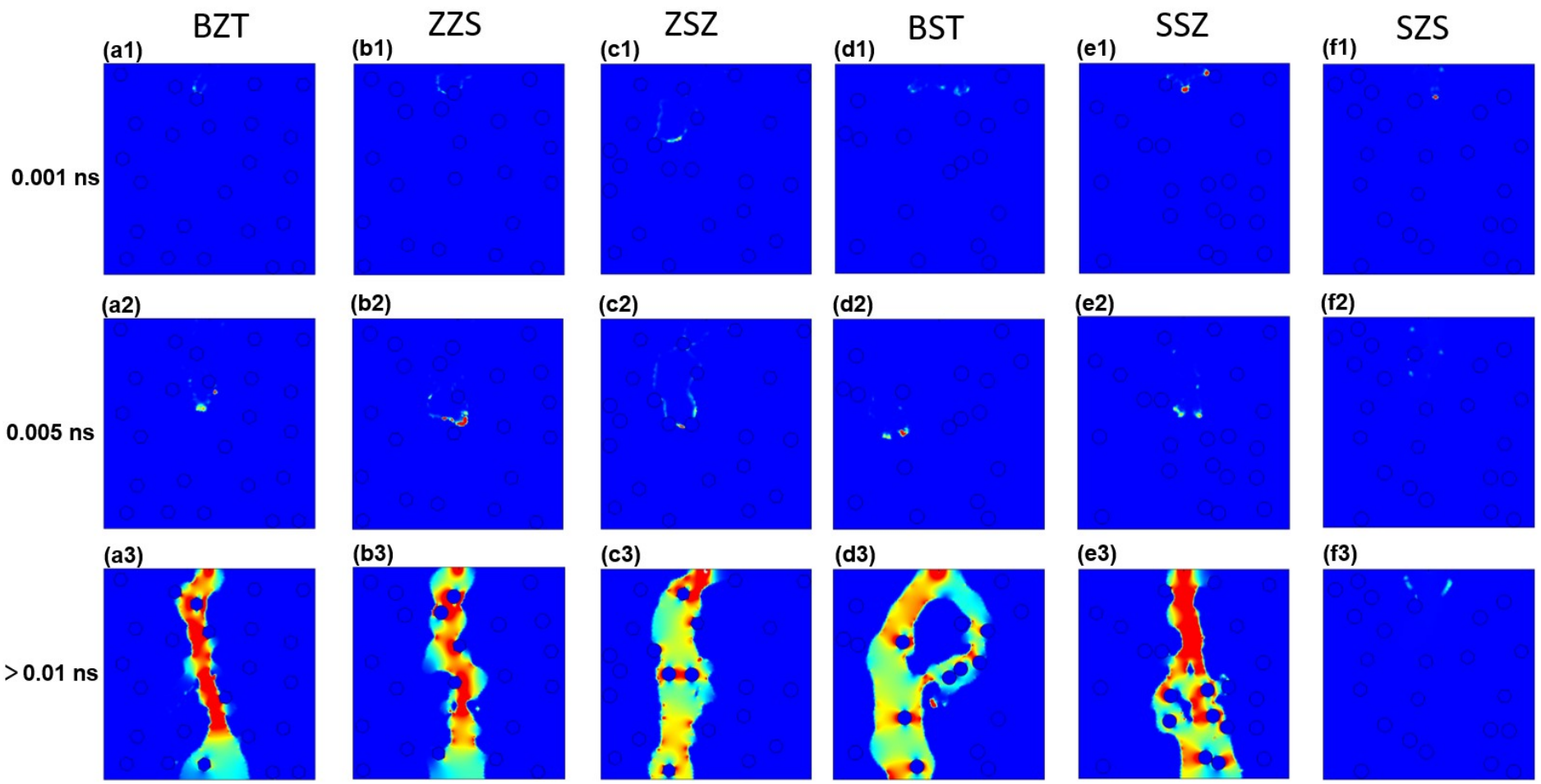

Fig. S5 the spread of the current density distribution of all the films under 6 MV/cm at different times after the voltage was applied.

8. Deduction of the Interfacial Polarization

The definition of polarization is shown in Eq. S19,

$$P=\chi_e\varepsilon_0 E \quad \text{Eq. S19}$$

where the E and P are the applied electrical field and the polarization obtained during the E, respectively. The χ_e is defined as susceptibility and can be written as:

$$\kappa=1+\chi_e \quad \text{Eq. S20}$$

where κ is the dielectric constant, which sometimes is also called relative electric permittivity, and the relationship between the permittivity (ε), relative electric permittivity (κ) and vacuum permittivity is (ε_0):

$$\varepsilon=\kappa\varepsilon_0 \quad \text{Eq. S21}$$

Combine Eq. S19-S21, we can have the relationship between P and ε of:

$$P=\varepsilon E(1-\frac{1}{1+\chi_e}) \quad \text{Eq. S22}$$

Considering The Clausius–Mossotti relation of:

$$1+\frac{3}{\chi_e}=\frac{3}{N\alpha} \quad \text{Eq. S23}$$

The N and α are the number of dipoles in a unit volume of a dielectric material and the molecular polarizability. The molecular polarizability should be an average value in a dielectric with different kinds of dipoles. The definition of dipole moment in dielectric shows the relationship between dipole moment of:

$$\alpha=\frac{ql}{\varepsilon_0 E_{local}} \quad \text{Eq. S24}$$

where the E_{local}, q, and l are the electrical field applied on each unit cell, the charge of the dipole, and the distance between the center of the positive charge and the center of the

negative charge in the dipole, respectively. When we combine the Eq. S19, Eq. S21 and Eq. S22, and finally, we can have:

$$P = \frac{3\varepsilon}{\frac{3\varepsilon_0}{N^2 q l} + \frac{2}{E}} \qquad \text{Eq. S25}$$

in which the polarization of a dielectric material under a certain electrical field positively correlates with the dipole density and the dipole moment.

In our work, the symmetrical structures of ZSZ and SZS have higher dipole density and, thus, higher polarization than the ZZS and SSZ, respectively, especially at higher electric field.

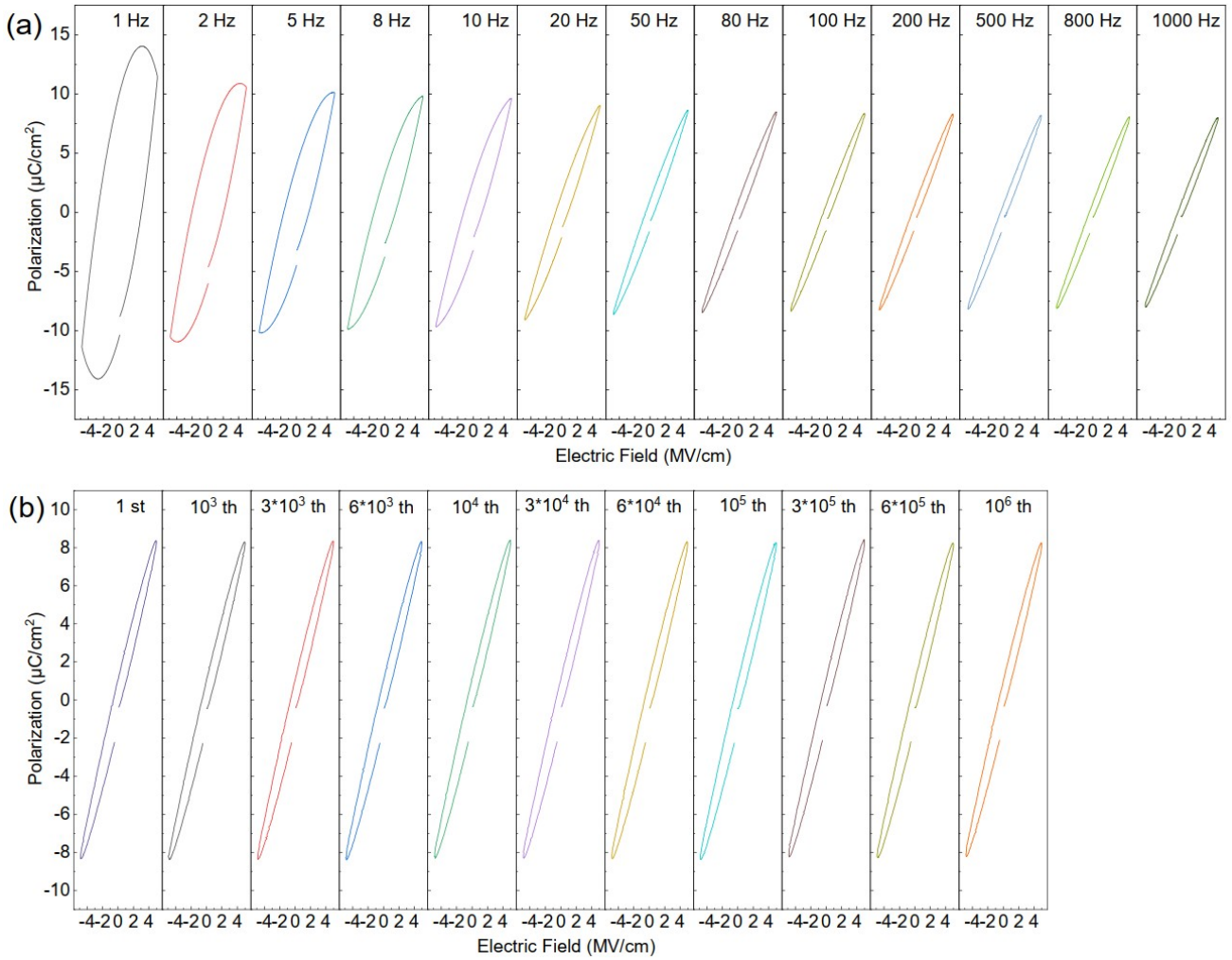

Fig. S6 (a) *P-E* loops of the SZS measured from 1 Hz to 1000 Hz under 5.0 MV/cm at room temperature; (b) *P-E* loops of the SZS obtained after polarization fatigue from the 1^{st} circle to the $10e6^{th}$ circle at room temperature.

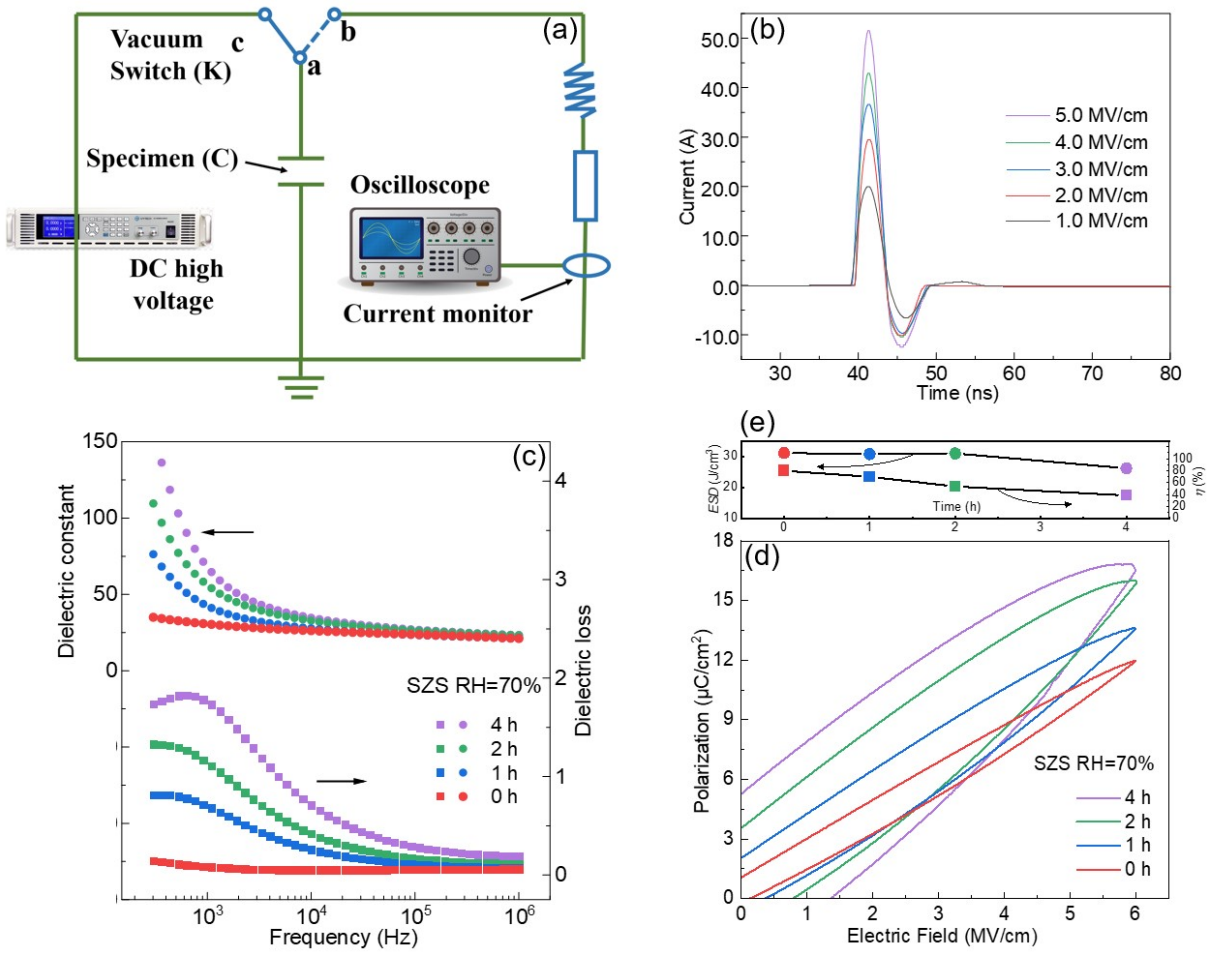

Fig. S7 (a) the R-L-C circuit for measuring the discharging performances of the SZS in our work; (b) the undamped discharge curves of the SZS under different applied electric fields at room temperature; (c) ε-f and *tanδ-f* curves; (d) *P-E* loops of the SZS after being kept in a humid environment (RH=70% & RT) for different times; (e) the corresponding *ESD* and *η* calculated from Fig. S7(d).

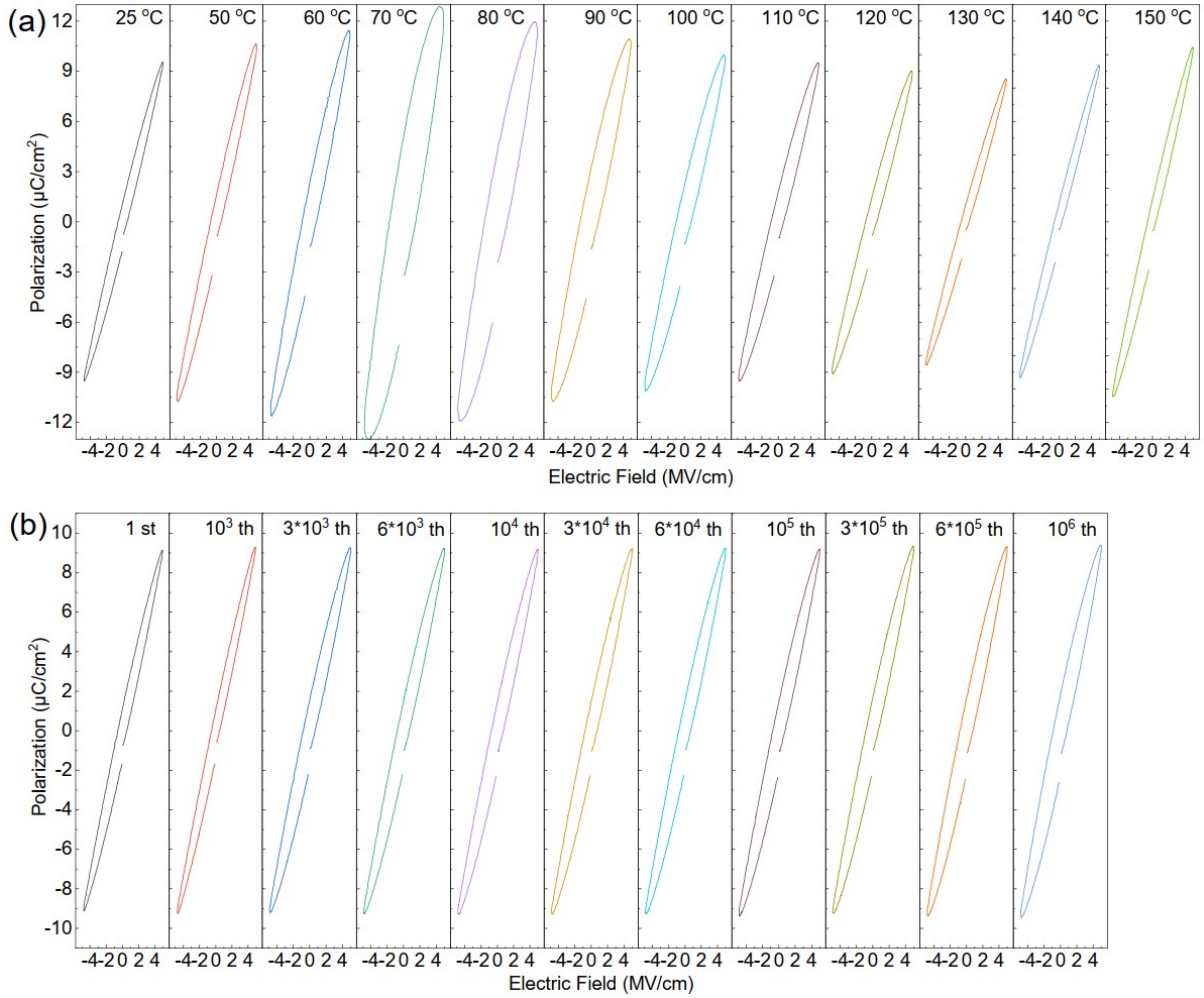

Fig. S8 (a) *P-E* loops of the SZS measured from 25 °C to 150 °C under 5.0 MV/cm; (b) *P-E* loops of the SZS obtained after polarization fatigue from the 1st circle to the 10e6th circle under 5.0 MV/cm at 150 °C.

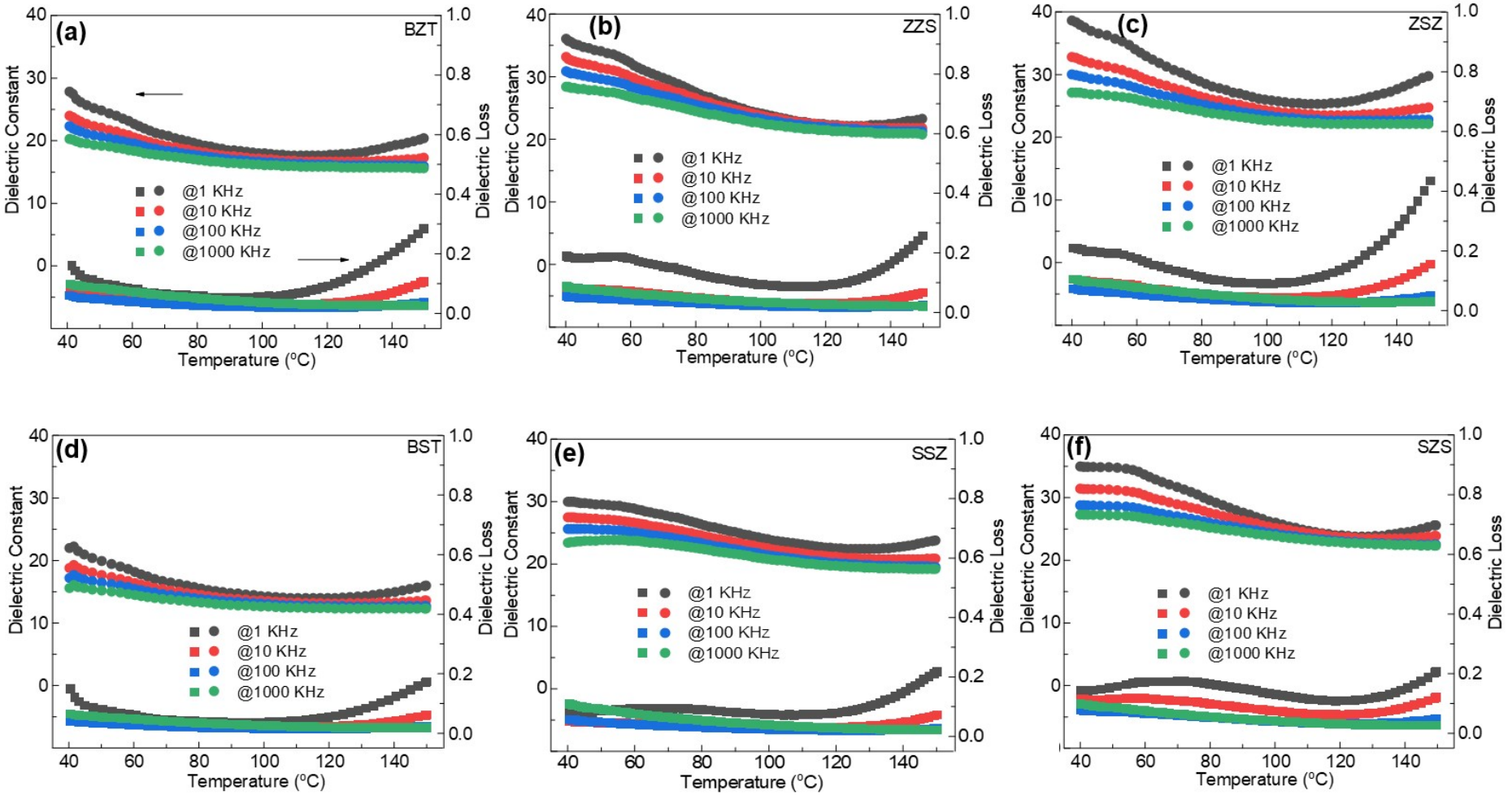

Fig. S9 the temperature-dependent of ε and *tan* δ of all the films in our work.

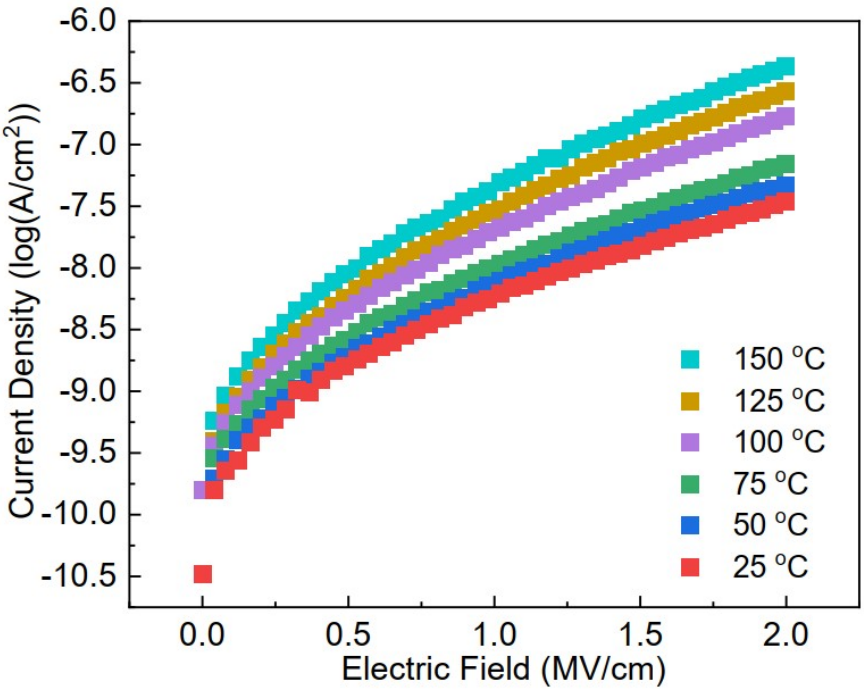

Fig. S10 the J-E curves of the SZS from room temperature to 150 °C

References

1. S. Zhang, J. Liu, Q. Guo, N. Wei, Y. Ning, Y. Bai, Y. Tian, T. Wang, Z. Sun, Y. Pu, *Composites Part A: Applied Science and Manufacturing*, 2023, **165**, 107329.
2. R.A. Young, "Pressing the Limits of Rietveld Refinement," Australian Journal of Physics 41(2), 297–310 (1988).
3. W. Li, Q. Meng, Y. Zheng, Z. Zhang, W. Xia and Z. Xu, Applied Physics Letters, *Applied Physics Letters*, 2010, 96, 19.
4. X. Ren, N. Meng, H. Zhang, J. Wu, I. Abrahams, H. Yan, E. Bilotti and M. J. Reece, *Nano Energy*, 2020, **72**, 104662.
5. Y. Xie, J. Wang, Y. Yu, W. Jiang and Z. Zhang, *Applied Surface Science*, 2018, **440**, 1150-1158.
6. P. Wang, Z. Pan, W. Wang, J. Hu, J. Liu, J. Yu, J. Zhai, Q. Chi and Z. Shen, *Journal of Materials Chemistry A*, 2021, **9**, 3530-3539.
7. Y. Cheng, Z. Pan, H. Chen, X. Ding, Z. Li, X. Fan, J. Liu, P. Li, J. Yu and J. Zhai, *Journal of Materials Chemistry A*, 2022, 10, 21650-21658.
8. H. Bai, K. Zhu, Z. Wang, B. Shen, J. Zhai, *Advanced Functional Materials*, 2021, 31, 2102646.
9. Y. Liu, J. Gao, R. Yao, Y. Zhang, T. Zhao, C. Tang and L. Zhong, *Materials Chemistry and Physics*, 2020, **250**, 123155.
10. M. Feng, C. Zhang, G. Zhou, T. Zhang, Y. Feng, Q. Chi and Q. Lei, *Ieee Access*, 2020, **8**, 81542-81550.
11. H. Bai, G. Ge, F. Yan, K. Zhu, J. Lin, C. Shi, J. Qian, Z. Wang, B. Shen, J. Zhai, *Energy Storage Materials*, 2022, **46**, 503-511.

12. Y. Niu, F. Xiang, Y. Wang, J. Chen and H. Wang, *Physical Chemistry Chemical Physics*, 2018, **20**, 6598-6605.
13. J. Jiang Z. Shen, J. Qian, Z. Dan, M. Guo, Y. He, Y. Lin, C. Nan, L. Chen, Y. Shen, *Nano Energy*, 2019, **62**, 220-229.
14. L. Jing, W. Li, C. Gao, M. Li and W. Fei, *Composites Science and Technology*, 2022, **227**, 109568.
15. R. Zhang, L. Li, S. Long, H. Lou, F. Wen, H. Hong, Y. Shen, G. Wang and W. Wu, *Journal of Materials Science: Materials in Electronics*, 2021, **32**, 24248-24257.
16. Q. Wang, J. Zhang, Z. Zhang, Yanan Hao and Ke Bi, *Advanced Composites and Hybrid Materials*, 2020, **3**, 58-65.
17. Q. Chi, Tao Ma, Y. Zhang, Q. Chen, C. Zhang, Y. Cui, T. Zhang, J. Lin, X. Wang and Q Lei, *ACS Sustainable Chemistry & Engineering*, 2018, **6**, 403-412.
18. J. Dong, J. Han, Y. Liu, A. Nakajima, S. Matsushita, S. Wei, and W. Gao, *ACS applied materials & interfaces*, 2014, **6**, 1385-1388.
19. J. Robertson, *Journal of Vacuum Science & Technology B*, 2000, **18**, 1785-1791.
20. M. Hikita, M. Nagao, G. Sawa and M. Ieda, *Journal of Physics D: Applied Physics*, 1980, **13**, 661.
21. N. Meng, X. Ren, G. Santagiuliana, L. Ventura, H. Zhang, J. Wu, H. Yan, M. J Reece and E. Bilotti, *Nature communications*, 2019, **10**, 4535.
22. J. Huang, Y. Zhou, Z. Zhou and R. Liu, *AIP Advances*, 2016.